

# Spin excitations and flat electronic bands in a Cr-based kagome superconductor

Received: 11 April 2025

Accepted: 17 July 2025

Published online: 14 August 2025

 Check for updates

Zehao Wang  <sup>1,20</sup>, Yucheng Guo  <sup>1,20</sup>, Hsiao-Yu Huang  <sup>2,20</sup>, Fang Xie  <sup>1,20</sup>, Yuefei Huang <sup>3</sup>, Bin Gao  <sup>1</sup>, Ji Seop Oh <sup>1,4,5,6</sup>, Han Wu  <sup>1</sup>, Jun Okamoto  <sup>2</sup>, Ganesha Channagowdra <sup>2</sup>, Chien-Te Chen  <sup>2</sup>, Feng Ye  <sup>7</sup>, Xingye Lu  <sup>8</sup>, Zhaoyu Liu  <sup>9</sup>, Zheng Ren  <sup>1</sup>, Yuan Fang  <sup>1</sup>, Yiming Wang <sup>1</sup>, Ananya Biswas <sup>1</sup>, Yichen Zhang  <sup>1</sup>, Ziqin Yue  <sup>1,10</sup>, Cheng Hu  <sup>11</sup>, Chris Jozwiak  <sup>11</sup>, Aaron Bostwick  <sup>11</sup>, Eli Rotenberg  <sup>11</sup>, Makoto Hashimoto  <sup>12</sup>, Donghui Lu  <sup>12</sup>, Junichiro Kono  <sup>1,3,13,14</sup>, Jiun-Haw Chu  <sup>9</sup>, Boris I. Yakobson  <sup>3</sup>, Robert J. Birgeneau  <sup>4</sup>, Guang-Han Cao  <sup>15</sup>, Atsushi Fujimori  <sup>2,16,17</sup>, Di-Jing Huang  <sup>2,18,19</sup> , Qimiao Si  <sup>1,14</sup> , Ming Yi  <sup>1,14</sup>  & Pengcheng Dai  <sup>1,14</sup> 

In the quest for topology- and correlation-driven quantum states, kagome lattice materials have garnered significant interest for their band structures, featuring flat bands (FBs) from the quantum destructive interference of the electronic wavefunction. Tuning an FB to the chemical potential could induce electronic instabilities and emergent orders. Despite extensive studies, direct evidence of FBs tuned to the chemical potential and their role in emergent orders in bulk materials remains lacking. Using angle-resolved photoemission spectroscopy, resonant inelastic X-ray scattering, and density functional theory, we show that the low-energy structure of the Cr-based kagome metal superconductor  $\text{CsCr}_3\text{Sb}_5$  is dominated by FBs at the Fermi level. We also observe low-energy magnetic excitations evolving across the low-temperature transition, largely consistent with the FB shift. Our results suggest that the low-temperature order contains a magnetic origin and that the kagome FBs may play a role in the emergence of this order.

Quantum materials with a large density of states, such as associated with flat bands (FBs), can display exotic quantum states. The FBs, when tuned to near the chemical potential, can provide a large amount of degenerate electronic states across the Brillouin zone (BZ) that are available to respond to interactions, hence leading to electronic instabilities and potential emergent electronic orders, such as magnetic order, charge-density-wave, and unconventional superconductivity<sup>1–7</sup>. While FBs near the Fermi level can be achieved through moire superlattices of magic-angle twisted bilayer graphene<sup>8–10</sup>, geometrically frustrated lattices such as the kagome and pyrochlore systems can also exhibit FBs from quantum interference of the electronic wavefunctions<sup>11–15</sup>. However, stabilizing a kagome lattice to bring these FBs into close proximity to

the  $E_F$  has been challenging, and establishing a relationship between FBs and the electronic/magnetic order has been particularly difficult.

For example, extensive experimental studies on the kagome lattice materials, including the binary 11 systems ((Fe,Co)Sn<sup>16–20</sup> and FeGe<sup>21–23</sup>), the 135 systems (AV<sub>3</sub>Sb<sub>5</sub><sup>24–31</sup> and ATi<sub>3</sub>Bi<sub>5</sub> (A = K, Rb, Cs)<sup>32–35</sup>), and the 166 systems (RMn<sub>6</sub>Sn<sub>6</sub> and RV<sub>6</sub>Sn<sub>6</sub> (R = rare earth)<sup>36–44</sup>), have revealed emergent orders, from quantum magnetism and unconventional superconductivity to nematicity and charge orders. However, these phases are often discussed in connection to characteristic features in the electronic structure, such as the Van Hove Singularities (VHSs) or Dirac fermions, attributed to the inherent topology of the kagome lattice, and not to the kagome FBs<sup>45–52</sup>. A noteworthy

A full list of affiliations appears at the end of the paper.  e-mail: [djhuang@nsrrc.org.tw](mailto:djhuang@nsrrc.org.tw); [qmsi@rice.edu](mailto:qmsi@rice.edu); [mingyi@rice.edu](mailto:mingyi@rice.edu); [pdai@rice.edu](mailto:pdai@rice.edu)

development in this context is the discovery of  $\text{Ni}_3\text{In}$ , which is reported to host a partial FB at the  $E_F$  by density functional theory (DFT) predictions and simultaneously exhibit non-Fermi liquid transport behaviors<sup>53</sup>. This finding bolsters the hypothesis that a FB at the  $E_F$  extending throughout the momentum space could be a promising avenue to realize exotic quantum orders in bulk quantum materials. Theoretically, models of  $d$ -electron systems on kagome and related lattices have been mapped to a Kondo lattice description through the notion of compact molecular orbitals, through which a phase diagram with emergent flat bands and strange metallicity has been identified<sup>54-56</sup>.

The chromium-based kagome metal  $\text{CsCr}_3\text{Sb}_5$  has recently been discovered and identified as a promising candidate<sup>57</sup>. Notably, this material exhibits phase transitions characterized by the appearance of superlattice peaks observed by X-ray diffraction (XRD) below  $T_{\text{CDW}} = 54$  K, suggested to be a unidirectional charge density wave (CDW) order. Magnetic susceptibility and nuclear magnetic resonance measurements indicate the simultaneous onset of a magnetic order<sup>57</sup>. First principle calculations reveal multiple competing density wave phases<sup>58,59</sup>. Under the application of hydrostatic pressure, the two orders are separated in temperature and suppressed, and a superconducting dome appears with a  $T_c$  peaking at 6.4 K<sup>57</sup>. Although the phase diagram is reminiscent of that of other known unconventional superconducting families such as the iron-based superconductors and cuprates, where superconductivity competes with static magnetic order<sup>6,60</sup>, there has not yet been an understanding of the nature of the competing order, nor evidence of FBs and their association with magnetism across the 54 K phase transition.

By combining polarization-dependent angle-resolved photo-emission spectroscopy (ARPES) measurements and DFT calculations, we unveil the presence of FBs near  $E_F$  extending through a large portion of the BZ. As the temperature is lowered across  $T_{\text{CDW}}$ , this FB exhibits a downward shift of approximately 20 meV away from the  $E_F$ . From resonant inelastic X-ray scattering (RIXS) experiments, we find clear non-dispersive magnetic excitations above the density wave transition temperature near the BZ center. The overall energy spread as well as the center energy position of the magnetic excitations show an increase below  $T_{\text{CDW}}$ , consistent with the observed shift in FBs from the ARPES measurements. Therefore, our combined ARPES and RIXS measurements signal that the low-temperature order contains a component that is magnetic in origin and that the associated excitations include electron-hole excitations of FBs, implying that FBs in the vicinity of the Fermi level play a role in the magnetic excitations in proximity to unconventional superconductivity<sup>6,61-63</sup>.

## Results

$\text{CsCr}_3\text{Sb}_5$  crystallizes in a layered hexagonal lattice consisting of alternately stacked Cr-Sb sheets and Cs layers (space group P6/mmm No. 191) with lattice parameters  $a = 5.4956(1)$  Å and  $c = 9.2602(2)$  Å at 293 K, where the Cr atoms form a kagome lattice (Fig. 1A). The characterization of  $\text{CsCr}_3\text{Sb}_5$  can be found in Supplementary Fig. S1. The corresponding 3D BZ is plotted in Fig. 1B. Figure 1C shows a map of the reciprocal space in the  $(H, K, 0)$  plane where superlattice peaks associated with the density wave order below  $T_{\text{CDW}}$  are marked. Our X-ray diffraction maps at 110 K (Fig. 1D) and 35 K (Fig. 1F) confirm the appearance of the superlattice peaks at  $(1/4, 0, 0)$  and  $(0, 1/4, 0)$  in the

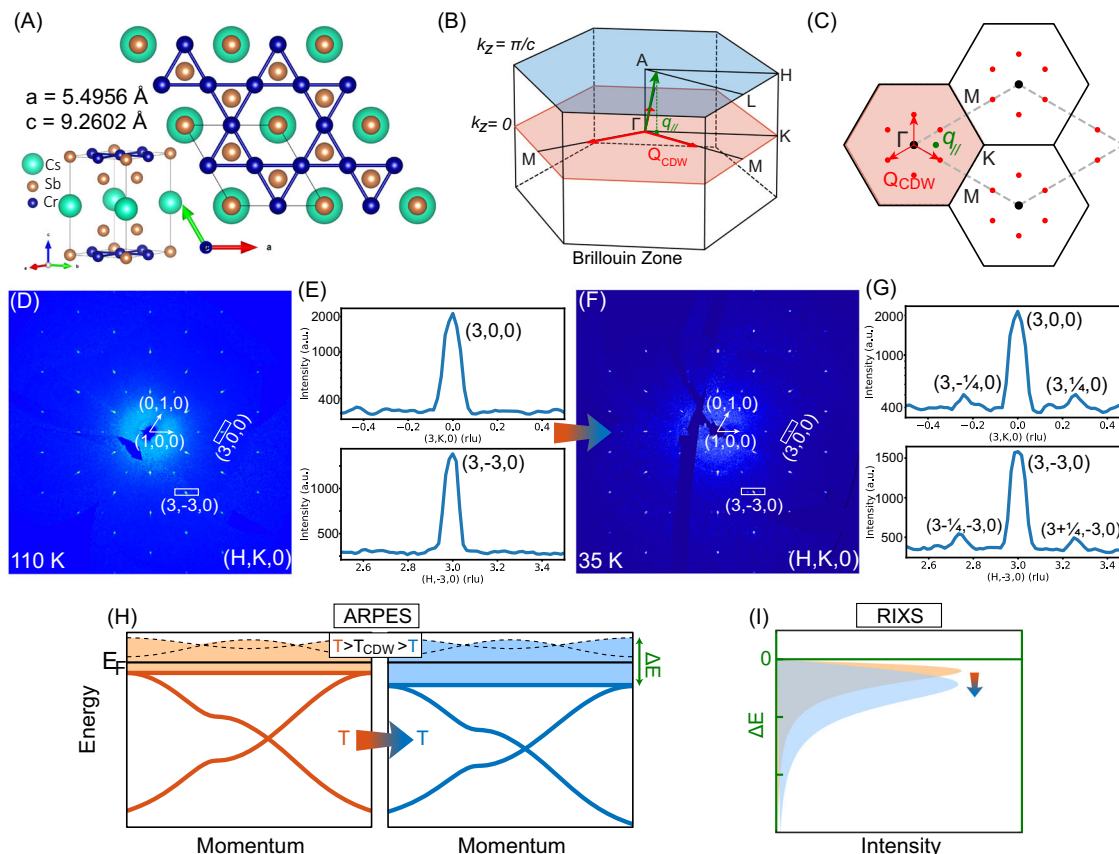
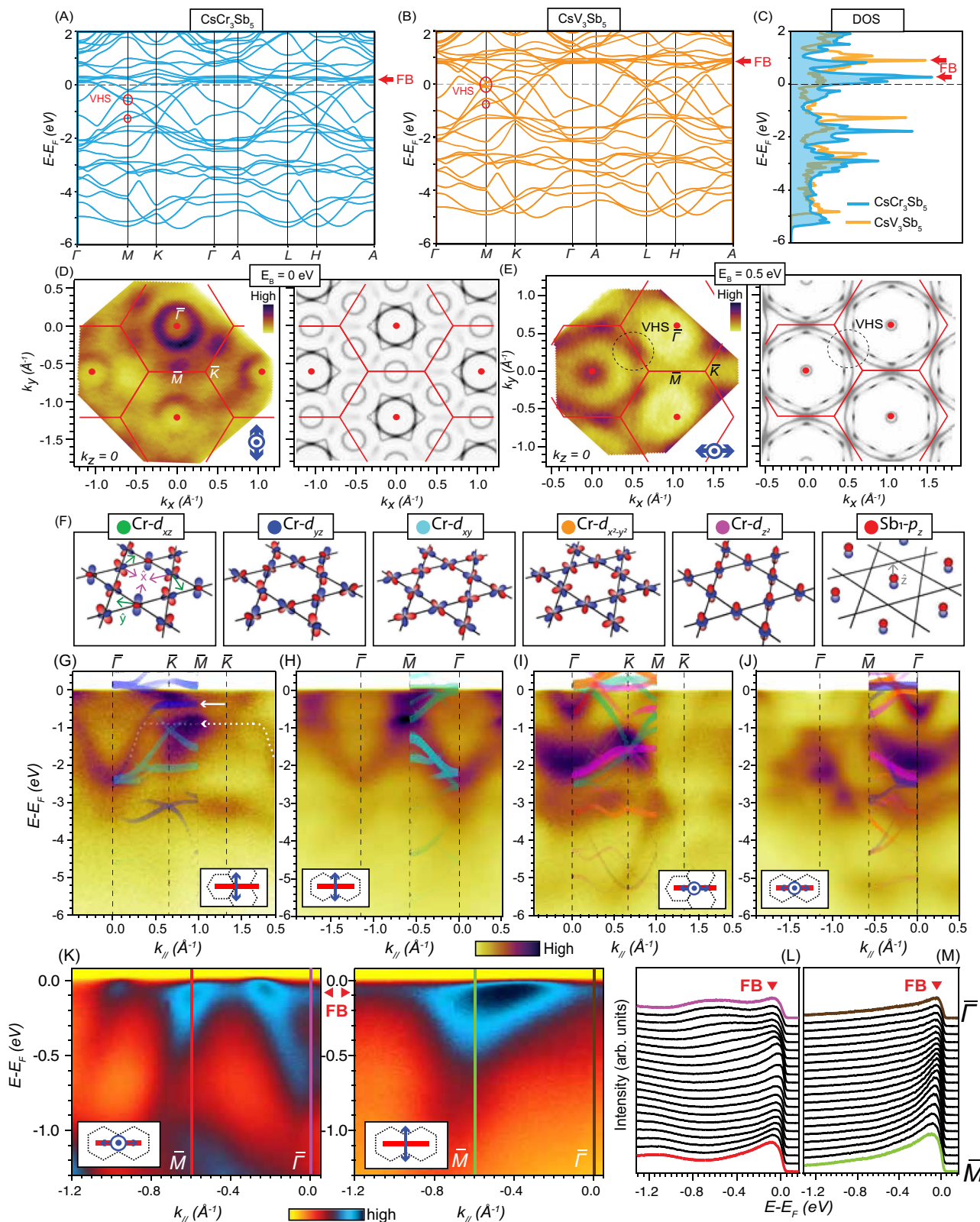


**Fig. 1 | Crystal structure, X-ray diffraction, Schematic of ARPES and RIXS results.** **A** Unit cell of  $\text{CsCr}_3\text{Sb}_5$ . The Cr forms a kagome lattice. **B, C** Reciprocal space of  $\text{CsCr}_3\text{Sb}_5$ . CDW observed by XRD are shown as red arrows or red points. The green arrow marks the  $q$  of temperature-dependent RIXS, where  $q_{\parallel}$  is the projection of  $q$  onto the sample surface. **D, F** XRD in the  $(H, K, 0)$  plane at 110 K and

35 K. **E, G** Corresponding cuts of (F) and (G), respectively. **H** Cartoon illustration of the ARPES observed shift of the kagome flat band away from  $E_F$  below  $T_{\text{CDW}}$ . **I** Cartoon illustration of the observed shift of the magnetic excitations observed by RIXS across  $T_{\text{CDW}}$ . The light orange and light blue shaded areas indicate the spectral weight that is coupled to particle-hole excitations across  $E_F$  illustrated in (H).



$(H, K, 0)$  plane below  $T_{CDW}$ <sup>57</sup>, as can be directly observed along the line cuts (Fig. 1E, G). We summarize our key findings in Fig. 1H, I. From ARPES measurements, we find FBs just  $\sim 60$  meV below the Fermi level that exhibit a  $\sim 20$  meV downward shift below  $T_{CDW}$  (Fig. 1H). Our RIXS measurements conclusively identify magnetic excitations near the BZ center with a spectral width of  $\sim 100$  meV. These excitations broaden and shift in energy below  $T_{CDW}$  (Fig. 1I), corresponding to a broadening

of the magnetic electron-hole excitations due to the temperature-dependent shift of the FBs away from the Fermi level. In the following, we present our detailed ARPES and RIXS experimental results.

As  $\text{CsCr}_3\text{Sb}_5$  is isostructural to the well-studied  $\text{CsV}_3\text{Sb}_5$ , we first compare the DFT calculated band structure of the two systems. As Cr has one additional valence electron,  $\text{CsCr}_3\text{Sb}_5$  has more electron filling than  $\text{CsV}_3\text{Sb}_5$ . This is reflected in the calculated band structure

**Fig. 2 | Electronic structure of  $\text{CsCr}_3\text{Sb}_5$ .** **A** DFT-calculated band structure of  $\text{CsCr}_3\text{Sb}_5$ . **B** DFT-calculated band structure of  $\text{CsV}_3\text{Sb}_5$ . In **(A)** and **(B)**, red arrows mark the energy position of the flat bands (FB) while red circles mark the positions of the VHSs in both  $\text{CsCr}_3\text{Sb}_5$  and  $\text{CsV}_3\text{Sb}_5$ . **C** Comparison of the DOS of  $\text{CsCr}_3\text{Sb}_5$  (cyan) and  $\text{CsV}_3\text{Sb}_5$  (orange), whose FB energy positions are indicated by the red arrows, respectively. **D** Fermi surface of  $\text{CsCr}_3\text{Sb}_5$  measured with 102 eV photons on the left and DFT calculation on the right. Red solid lines mark the 2D projected BZ. Blue arrows denote the light polarization. **E** Same as **(D)** but at  $E_B = 0.5$  eV. The black dashed circles mark the position of the VHS at the M point. **F** The definition and illustration of the orbitals in  $\text{CsCr}_3\text{Sb}_5$ . **G–J** band dispersion taken with 114 eV **(G)(H)** LV and **(I)(J)** LH polarization along the

$\bar{\Gamma}\text{--}\bar{K}\text{--}\bar{M}$  and  $\bar{\Gamma}\text{--}\bar{M}\text{--}\bar{\Gamma}$  directions. The DFT calculations projected onto the orbitals observable in each measurement geometry, according to the selection rules, are overlapped on the band dispersions for comparison. Blue arrows denote the polarization direction. The white solid arrow denotes the  $d_{yz}$  character band position, while the white dashed arrow denotes its position in the observation, suggesting a possible orbital-selective band renormalization for  $d_{yz}$  orbitals. **K** Band dispersions measured with 100 eV photons ( $k_z = 0$ ) along  $\bar{\Gamma}\text{--}\bar{M}$ . The measurement geometry and polarization are as marked. **L** EDCs stacking in band dispersions taken with LH polarization at in **(K)**. **M** Same as **(L)** but taken with LV polarization. Lines of the same colors in **(K–M)** denote high symmetry point positions.

(Fig. 2A, B), where the main features in the two systems are qualitatively similar except an overall raised chemical potential in  $\text{CsCr}_3\text{Sb}_5$  compared to that of  $\text{CsV}_3\text{Sb}_5$ . In particular, the kagome FBs in  $\text{CsCr}_3\text{Sb}_5$  are much closer to  $E_F$ , positioned approximately 200 meV above the  $E_F$ , in contrast to around 1 eV for  $\text{CsV}_3\text{Sb}_5$ . Also, the VHSs lie well below  $E_F$  for  $\text{CsCr}_3\text{Sb}_5$ , while  $\text{CsV}_3\text{Sb}_5$  hosts multiple VHSs near  $E_F$ . The difference in the predicted FB position is also pronounced in the density of states (DOS) calculations, highlighted by red arrows in Fig. 2C. To visualize the electronic structure of  $\text{CsCr}_3\text{Sb}_5$ , we present ARPES results measured at 10 K on a kagome termination dominant surface (see core level measurement in the SM and Supplementary Fig. S2). The Fermi surface map corresponding to the  $k_z = 0$  plane is shown in comparison to that calculated from DFT (Fig. 2D). Noticeably, the Fermi surfaces contain a large pocket around the  $\bar{\Gamma}$  point and small pockets around the M points, in good alignment with the DFT calculations for the phase without the density wave order. To note, no remarkable band folding was observed on the Fermi surface. Meanwhile, the VHSs at the M points are observed at 0.5 eV below  $E_F$ , evident in the characteristic triangular pockets around the K points with their corners touching at the M points, giving a good overall agreement with the DFT calculations (Fig. 2E).

To further visualize the electronic structure of  $\text{CsCr}_3\text{Sb}_5$  and understand its orbital textures, we present a detailed comparison between band dispersions along high symmetry directions and the orbital-projected DFT in Fig. 2. The low-energy electronic states are mostly populated by the five Cr-3d orbitals and Sb-5p orbitals illustrated in Fig. 2F. We adopt the site-dependent local coordinates as the basis shown by the colored arrows to fully respect the lattice symmetry (see SM Supplementary Fig. S3). Orbital-projected DFT calculations of the band structure along the high symmetry directions suggest that the topological flat bands associated with the kagome lattice are predominantly of  $d_{xz}$  and  $d_{yz}$  orbital character, immediately above  $E_F$  (see SM Supplementary Fig. S3). Experimentally, we can utilize the polarization-dependent photoemission matrix elements to gain information on the dominant orbital character of the observed dispersions. Based on a detailed analysis of such matrix elements for all of our measurement geometries (see SM Supplementary Fig. S3), we can overlay the orbital-projected calculated bands from symmetry-allowed orbitals along two high symmetry directions in the BZ under two polarization directions (Fig. 2), while raw data without DFT is provided in the SM Supplementary Fig. S6). While most features exhibit reasonable overall agreements, we notice that there is a portion of a flat dispersion between  $\bar{K}\text{--}\bar{M}$  near  $-1$  eV (dotted white arrow in Fig. 2I) connected to an electron band towards  $\bar{\Gamma}$ . The orbital selection rules suggest these features can be attributed to  $d_{yz}$  or  $d_{xy}$  orbital characters (see SM Supplementary Fig. S3). However, no bands in the DFT calculations match this flat portion. To capture this feature, we note that if a renormalization factor of 1.4 is applied to the  $d_{yz}$  character band marked by the solid white arrow, the agreement can be better established (see SM Supplementary Fig. S4). Another possibility that we cannot rule out is that the flat portion of  $d_{xy}$  character near  $-2$  eV being strongly renormalized. In either scenario, orbital-dependent correlation effects would need to be invoked in  $\text{CsCr}_3\text{Sb}_5$ , which is not

uncommonly found in multi-orbital systems, including the iron-based superconductors<sup>64–67</sup>, a recently reported Mn-based kagome system<sup>68</sup>, as well as  $\text{Ca}_{1-x}\text{Sr}_x\text{RuO}_4$ <sup>69</sup>.

Having discussed the overall electronic structure, we next focus on the FB near  $E_F$ . First, from the orbital-projected band structure calculated by DFT, we see that the kagome topological flat band appears at 0.25 eV above  $E_F$ . In Fig. 2K–M, we present the measured band dispersions within 1 eV of  $E_F$  along  $\bar{\Gamma}\text{--}\bar{M}$  measured under different polarizations together with the energy distribution curves (EDC). Interestingly, for both polarizations, a flat band feature close to  $E_F$  can be observed. This can be seen in the ubiquitous peak in the EDCs within 100 meV of  $E_F$ , and is especially clear at the  $\bar{\Gamma}$  point marked by the red arrows, where according to the DFT calculations, should only have an electron band near  $E_F$  (Fig. 2A). The location of the electron band bottom can be seen in the EDCs at  $\bar{\Gamma}$  in the form of a hump near  $-0.7$  eV. The only feature above the electron band in the DFT calculation is the kagome flat band, situated slightly above  $E_F$ . Hence, if we assume that the DFT results are reasonably accurate, the peak we observe in all the EDCs at  $\bar{\Gamma}$ , located between the electron band bottom and  $E_F$ , must be the kagome flat band that has been brought down from above  $E_F$ .

Furthermore, considering that the FB is observable under all of the polarization geometries (see SM and Supplementary Fig. S9 for the complete set of measurements), including those that only allow either even or odd parity orbitals to be observed, this suggests that both  $d_{xz}$  and  $d_{yz}$  orbitals are participating in forming the observed FB. An additional confirmation for the observation of the FB below  $E_F$  can be noted from the electron band at  $\bar{\Gamma}$ . This Sb  $p_z$ -dominated band is also seen in  $\text{CsV}_3\text{Sb}_5$ , albeit with a shallower band bottom due to the smaller electron filling<sup>70</sup>. However, distinct from the  $\text{CsV}_3\text{Sb}_5$  case, we observe a bending of the electron dispersion near  $-70$  meV in  $\text{CsCr}_3\text{Sb}_5$  (Fig. 2K). From the DFT calculations, it is clear that this electron band hybridizes with the kagome flat band where they cross (see SM and Supplementary Fig. S9). Since the energy position of this slope change matches with the observed peak in the EDCs, this is an indication of the hybridization of the FB with the electron dispersion. We note that while electron-boson coupling generically could also result in dispersion kinks, in such situations, a broadening of the imaginary part of the self-energy beyond the mode energy must also accompany the modification of the real part of the self-energy. Since we do not observe such broadening, we can definitively exclude electron-boson coupling as a potential cause of such dispersion bending (see Supplementary information S9 for detailed analysis). The observed hybridization of the flat band with the electron band further confirms that the FB we observe is intrinsic, not due to disorder-induced localized states that do not interact with the intrinsic band structure. The observation of this hybridization kink also confirms that the peak we observe in the EDC is not due to spectral weight leaking from an FB located above  $E_F$ , but rather an FB that is located below  $E_F$ .

Having identified the kagome flat bands, we next present our RIXS results to reveal the low-energy excitations. While ARPES measures the single-particle spectral function in momentum space ( $\mathbf{k}$ ), RIXS measures two-particle excitations in momentum transfer  $\mathbf{q} = \Delta\mathbf{k}$ , such as magnetic excitations, phonons, crystal-field excitations and plasmons<sup>71</sup>.

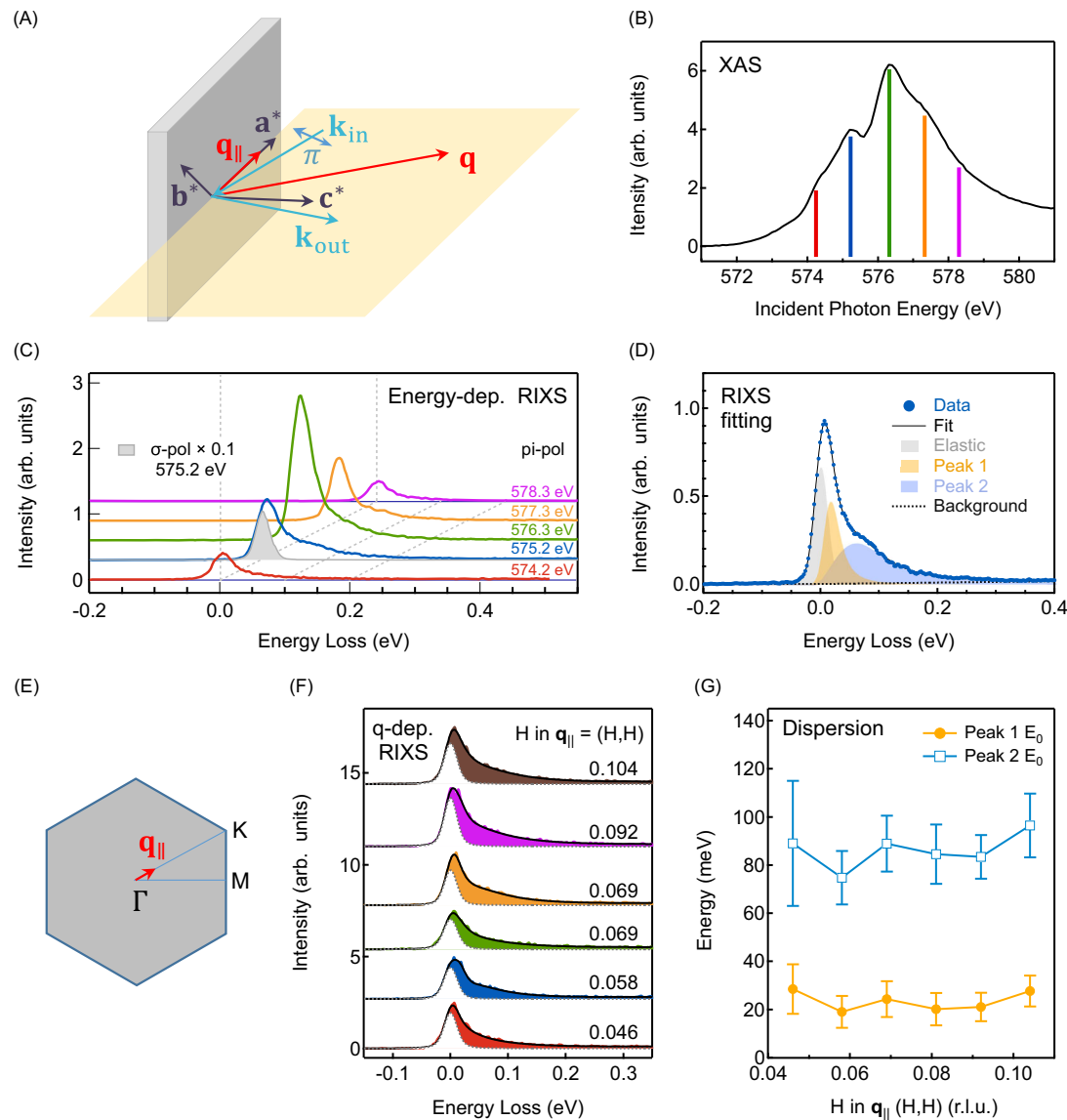


**Fig. 3 | RIXS measurements.** **A** Illustration of RIXS scattering geometry. The scattering plane was perpendicular to the  $ab$  plane of  $\text{CsCr}_3\text{Sb}_5$ . The incident and scattered wave vectors of X-rays, i.e.,  $\mathbf{k}_{\text{in}}$  and  $\mathbf{k}_{\text{out}}$ , are orthogonal. The polarization of incident X-rays was in the scattering plane, i.e.,  $\pi$ -polarized, resulting in RIXS with a cross-polarization geometry. The polarization of scattered X-rays was unresolved. The projection of wavevector change  $\mathbf{q}$  onto the  $ab$  plane is denoted as  $\mathbf{q}_{\parallel}$ . **B** Cr  $L_3$ -edge X-ray absorption spectrum (XAS) of  $\text{CsCr}_3\text{Sb}_5$  recorded at 300 K. Colored vertical bars indicate the X-ray energies used in RIXS measurements. **C** Incident-energy-dependent RIXS with  $\mathbf{q}_{\parallel}$  along the  $\Gamma$ /M direction at 25 K. Spectra in color were recorded with  $\pi$ -polarized X-rays at selected energies. The RIXS spectrum with  $\sigma$  polarization, i.e., X-ray

polarization perpendicular to the scattering plane, shows the instrumental energy resolution of RIXS. **D** Demonstration of curve fitting for RIXS data analysis. In addition to a linear background, a measured RIXS spectrum was fitted to a spectral profile consisting of three components: one elastic and two electronic excitations. See SM for fitting details. **E** First Brillouin zone in the  $a^*b^*$  plane of reciprocal space. The red arrow indicates  $\mathbf{q}_{\parallel}$  of momentum-dependent RIXS measurements. **F** Momentum-dependent RIXS with  $\mathbf{q}_{\parallel}$  along  $\Gamma$ /K at 25 K. The energy of incident photons was set to 575.2 eV to optimize the shoulder feature. The dashed lines plot the elastic components; the colored shades indicate spectral profiles arising from spin excitations. **G** Dispersion of  $E_0$  of two spin excitations as a function of in-plane momentum  $\mathbf{q}_{\parallel}$ .

The nature of the excitations can be determined by polarization analysis. Specifically, magnetic excitations can be conclusively determined when the scattered photons have rotated polarization from the incident beam<sup>72</sup>. Such excitations have been observed in cuprates via cross polarization RIXS measurements<sup>73–76</sup>. Figure 3A illustrates the scattering geometry of our RIXS experiments. To conclusively determine spin excitations of the system and exclude other excitations, we used  $\pi$ -polarized light with 90° scattering angle between the incident and scattered X-rays of wave vectors  $\mathbf{k}_{\text{in}}$  and  $\mathbf{k}_{\text{out}}$ , respectively. As the dominant low-energy electronic states of  $\text{CsCr}_3\text{Sb}_5$  are derived from Cr 3d orbitals, we carried out Cr  $L_3$ -edge RIXS to unravel its low-energy excitations. Figure 3B plots the X-ray absorption spectra across the Cr  $L_3$ -edge and shows X-ray energies at which RIXS measurements were

taken. Figure 3C plots the RIXS spectra of  $\text{CsCr}_3\text{Sb}_5$  taken at these different incident photon energies. The 90°-scattering geometry with  $\pi$ -polarized X-rays ensures the measurement of spin excitations. A clear spectral feature of spin excitation appears around 70 meV as a shoulder of elastic scattering. This energy is smaller than the spin excitation energy scales of the iron<sup>61</sup> and copper-oxide superconductors<sup>62,77</sup>.

To quantitatively determine the energy scale of the spin excitations in  $\text{CsCr}_3\text{Sb}_5$ , we used a general damped harmonic oscillator model to generate the spectral profile of the spin excitations<sup>78,79</sup>

$$S(\mathbf{q}_{\parallel}, E) = A \frac{E_0}{1 - e^{-\beta E}} \frac{2\gamma E}{(E^2 - E_0^2)^2 + (\gamma E)^2}, \quad (1)$$

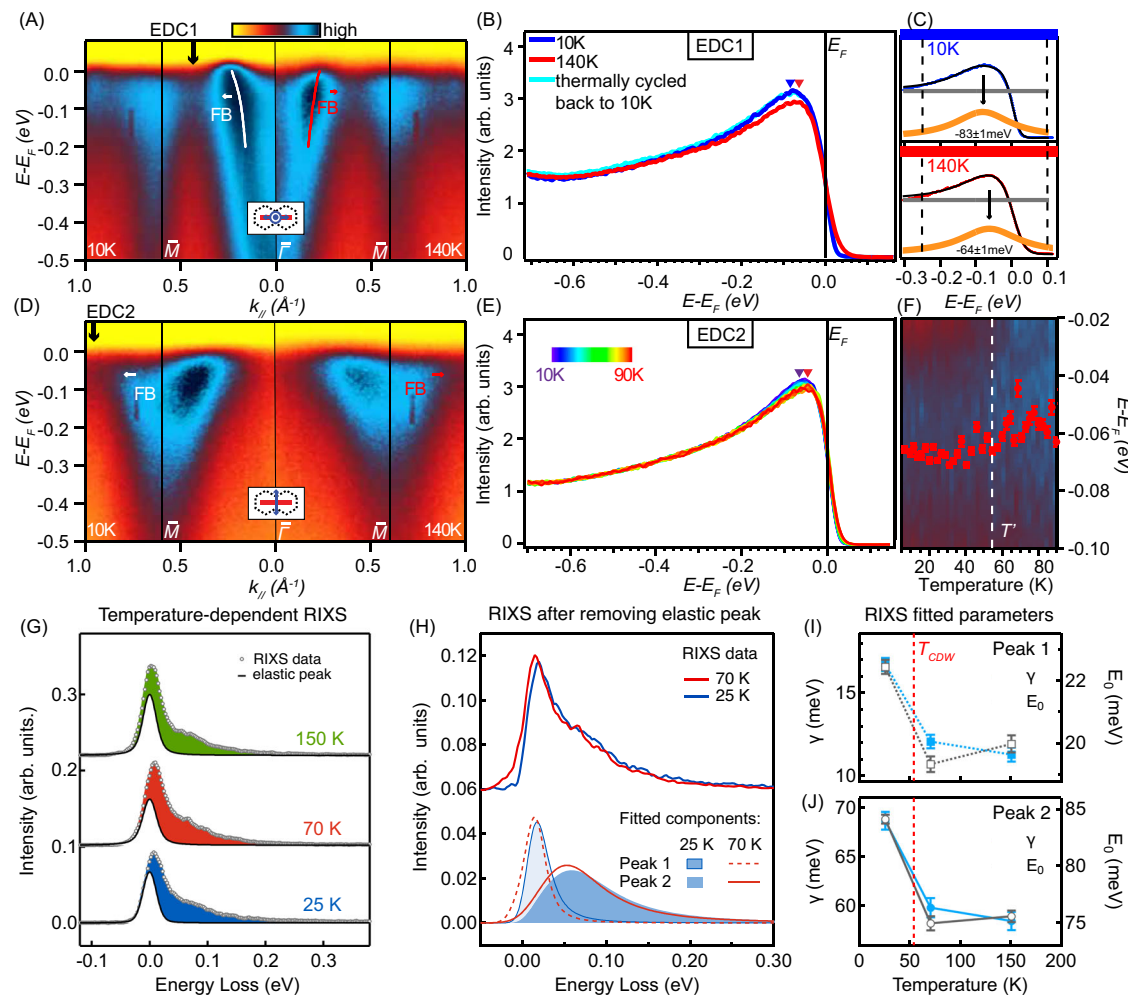


**Fig. 4 | Temperature-dependent results of ARPES and RIXS.** **A** Band dispersion taken with 114 eV LH polarization and horizontal slit direction at 10 K (left) and 140 K (right). White (10 K) and red (140 K) dots denote the fitted MDC positions (see SM) for the electron pocket at  $\Gamma$ . The arrows mark a kink in the dispersion, indicating hybridization with the FB. **B** EDC1 measured at the denoted position in (A) at 10 K, 140 K, and then thermally cycled back to 10 K. **C** Fitting details for the 10 K and 140 K EDC1 where a Lorentzian peak (orange) and a constant background (gray) are multiplied by the Fermi-Dirac (FD) function convolved with a fixed Gaussian peak of 40 meV Full-Width-Half-Maximum (FWHM) mimicking the experimental resolution. Blue/red dots are the raw data points, the same as (B). Vertical dashed lines mark the fitting range. The dashed arrows denote the fitted Lorentzian peak positions. **D** Same as (A) but measured with LV polarization.

**E** EDC2 as marked in (D) measured from 10 K to 90 K. **F** Fitted FB positions from EDCs after dividing the FD function convolved with a Gaussian peak with 40 meV FWHM. The dotted line marks the transition  $T_{CDW}$  previously reported<sup>57</sup>.

**G** Temperature-dependent RIXS. Open circles depict raw RIXS data measured with  $\pi$ -polarized incident X-rays at an energy of 572.5 eV and temperatures of 25, 70, and 150 K; solid lines plot the fitted elastic components. The shaded areas denote RIXS features arising from spin excitations. **H** RIXS spectra at 25 K (blue) and 70 K (red) after removing the elastic component. The bottom panel compares their fitted components of spin excitations. **I, J** Evolution of fitted parameters  $E_0$  and  $\gamma$  for temperatures changed across  $T_{CDW}$ . The vertical dashed line indicates the CDW transition temperature  $T_{CDW}$ .

where  $E_0$  is the undamped energy,  $\gamma$  the damping factor,  $\beta = \frac{1}{k_B T}$  ( $k_B$  is the Boltzmann constant) and  $A$  is a constant. The elastic peak was modeled using a Voigt function, with its spectral width determined by the instrumental resolution. The contribution from the fluorescence tail was described with a polynomial function. Since the spectral profile around zero energy was wider than the instrumental resolution, a low-energy component of spin excitation was required to fit the data. Therefore, the measured RIXS spectrum was fitted to a spectral profile comprising three components: one elastic peak, two electronic excitations and one polynomial background, as shown in Fig. 3D. We note that we cannot describe the finite energy electronic excitations with a single peak because the overall fit would then require elastic scattering much larger than the instrumental resolution (see Supplementary Information S10).

We also measured momentum-dependent RIXS with  $q_{\parallel}$  along  $\Gamma - K$  (Fig. 3E) to further verify that the observed electronic excitations arise from transitions involving FBs. Figure 3F summarizes the

$q_{\parallel}$  dependence of the magnetic excitations within the available momentum transfer range along the  $[H, H, 0]$  direction. The fitted undamped energy  $E_0$  of the two spin components in our RIXS data shows no dispersion for all  $q_{\parallel}$  within the available range, as plotted in Fig. 3G. This is consistent with the FB results concluded from ARPES measurements.

Finally, we present the temperature dependence of the FBs and spin excitations across  $T_{CDW}$ . In Fig. 4A we compare the band dispersion along  $\Gamma - M$  taken with linear vertical (LV) polarization at 10 K (left) and 140 K (right). This experimental setup selects the FB of  $d_{yz}$  orbital (See SM Supplementary Fig. S7). The FBs are visible at both temperatures, as seen in the spectral image, the peak in the EDC, as well as from the bend in the fitted electron dispersion (marked by a white and red arrow, respectively). From the spectral image, the location appears to be closer to  $E_F$  at 140 K compared to 10 K. This can be seen better from the direct comparison of the EDC taken at the location marked by the black arrow: the peak is shifted towards  $E_F$  at

140 K by about 20 meV, and is recovered after thermally cycling back to 10 K. The direction of the shift is opposite to that expected purely from the thermal broadening effect of the Fermi-Dirac distribution and hence indicates a real shift of the FB. Similarly, the comparison of band dispersion along  $\bar{\Gamma}-\bar{M}$  taken with linear horizontal (LH) polarization and horizontal slit at 10 K ( $T < T_{CDW}$ ) and 140 K ( $T > T_{CDW}$ ) shows that FB of  $d_{xz}$  orbital also shift towards  $E_F$  (Fig. 4E). We provide the continuous temperature evolution of this shift and the fitting result in Fig. 4F with the detailed temperature evolution presented in Fig. 4E. Additional temperature dependence measurements and data analysis are given in the Supplementary Information and Supplementary Fig. S6.

We also conducted temperature-dependent RIXS measurements at temperatures across  $T_{CDW}$ . Figure 4G presents the measured RIXS spectra within an energy range of 0.3 eV. All spectra were analyzed using the same curve-fitting scheme as shown in Fig. 3D. To highlight the spectral changes, Fig. 4H compares RIXS spectra above and below  $T_{CDW}$  after removing elastic scattering, revealing a subtle yet distinct broadening and shift towards higher energy as the temperature is cooled across  $T_{CDW}$ . For quantitative analysis, Fig. 4I, J show the evolution of the fitted bare energy  $E_0$  and damping factor  $\gamma$  of both spin excitations, which align with ARPES results shown in Fig. 4F. The observed excitations are coupled to the electron-hole excitations across the Fermi level. As such, the broadening and shifting of the spin excitations likely reflect the shifting of the FBs away from  $E_F$ , both below and above  $E_F$ .

## Discussions

First, from our systematic polarization dependence ARPES measurements, we clearly resolve the presence of the kagome flat bands near  $E_F$  in  $\text{CsCr}_3\text{Sb}_5$ . In comparison to the isostructural  $\text{CsV}_3\text{Sb}_5$ , the Cr system is effectively electron-doped to an extent that, at the DFT level, the kagome flat bands are brought much closer to  $E_F$ . However, our observations indicate that bare DFT does not accurately reproduce the flat bands below  $E_F$ . When the necessary correlation corrections are applied, the discrepancies in the flat band position can be reconciled at a qualitative level, although improved sample quality and refined theoretical approaches are encouraged to further resolve this matter<sup>80,81</sup>. This is reminiscent of the flat band observed in the 3D pyrochlore material  $\text{CuV}_2\text{S}_4$ , where the destructive interference and orbital-selective correlation effects work in tandem to pin the flat bands to  $E_F$ <sup>82</sup>. It is also in line with the theoretical notion of emergent flat bands, the anticipated quantum phase transitions and strange metallicity<sup>54–56</sup> and, by extension, unconventional superconductivity.

Second, since the temperature-dependent shift of the FBs away from the Fermi level observed by ARPES across  $T_{CDW}$  is largely consistent with the increase in both the spin excitation energy and bandwidth observed by RIXS near the  $\bar{\Gamma}$  point, our results taken together provide compelling evidence that spin excitations probed by RIXS are coupled to the quasiparticle excitations of the FBs near the Fermi level. From previous X-ray diffraction experiments, it is clear that a structural phase transition occurs below  $T_{CDW}$  in  $\text{CsCr}_3\text{Sb}_5$ <sup>57</sup>. Our RIXS results indicate that this transition is also associated with changes in spin excitations. Hence, this transition is likely a composite order that involves both structural and magnetic degrees of freedom, potentially analogous to the structural and spin density wave order in the iron-pnictide superconductors<sup>61</sup>, which calls for future neutron scattering experiments to elucidate.

Third, we discuss the potential mechanism for the involvement of the kagome FBs in the formation of this electronic order. Since the chemical potential of  $\text{CsCr}_3\text{Sb}_5$  happens to be near the kagome FBs, it is conceivable that their presence drives an electronic order that pushes the FBs away from the Fermi level, as we have observed. With

hydrostatic pressure, this electronic order is suppressed, which would leave residual density of states from the FBs near  $E_F$  to experience the quantum fluctuations expected near a quantum critical point and potentially enable superconductivity. Moreover, unlike the pinning of the large DOS to the M points of the BZ for the VHSs in a kagome metal, the kagome FB provides a high density of states across a much larger portion of the BZ. Therefore, they could be susceptible to multiple types of electronic instabilities of similar energy scales and different  $q$ 's, which may be a cause for the involvement of both the lattice and spin degrees of freedom. It remains interesting to theoretically map out the competing orders promoted by the FBs that develop near- $E_F$  region in  $\text{CsCr}_3\text{Sb}_5$ .

Finally, it is interesting to compare  $\text{CsCr}_3\text{Sb}_5$  to the other known kagome metal systems that have been extensively studied. First,  $\text{AV}_3\text{Sb}_5$  and FeGe are both kagome metals that exhibit charge orders with an in-plane periodicity of  $2 \times 2$ . Both these systems exhibit the VHSs at the M points of the BZ in the proximity of  $E_F$ . While nesting is unlikely to be the dominant driving mechanism for the charge order as theoretically predicted, it may still be a necessary but insufficient condition for selecting the  $q$  for the  $2 \times 2$  charge order in these systems. In particular,  $\text{AV}_3\text{Sb}_5$  has no magnetism from  $3d$  electrons but has coexisting superconductivity and charge order, while FeGe has a strong coupling of a charge density wave and magnetic order but no superconductivity<sup>83,84</sup>.  $\text{CsCr}_3\text{Sb}_5$  appears to be special as suppression of the density wave by hydrostatic pressure drives strange metallicity and induces superconductivity<sup>57</sup>.

For kagome metals where the flat bands are in the vicinity of the Fermi level, there are two regimes where materials have been studied.  $\text{Ni}_3\text{In}$  represents a regime where the flat band is in proximity to  $E_F$  yet not readily observed by photoemission. In this regime, no electronic orders are formed yet, but the system exhibits non-Fermi liquid transport behavior, indicating proximity to a potential quantum critical point<sup>53</sup>. Arguably in the opposite limit is the category of compounds that exhibit strong ordered magnetism. Kagome magnets, including FeSn, FeGe, and the Mn- and Fe-based 166 systems all exhibit magnetism with ordering temperatures well above room temperature<sup>16,21,37,85,86</sup>. The electronic structure of these compounds, when calculated for the paramagnetic state, all show kagome flat bands that live in the vicinity of the Fermi level, which in the magnetically ordered state split via the exchange splitting, often with an energy scale of 1–2 eV<sup>21</sup>. However, recent work on FeSn thin film that measures its electronic structure through its magnetic ordering temperature reveals that the exchange splitting of the bands remains largely intact above the magnetic ordering temperature, demonstrating that the origin of the magnetism in this system is local in nature<sup>87</sup>, which is likely common for these Fe- and Mn-based system with exceptionally high ordering temperatures.

$\text{CsCr}_3\text{Sb}_5$  is clearly different. Cr-based systems are typically magnetic, but more itinerant than Fe- and Mn-based systems. The similarity of the measured dispersions in the low-temperature density wave ordered phase to the DFT calculated band structure of the non-ordered phase indicates that the modification of the electronic structure through this order is subtle. This is not uncommon for systems with electronically driven orders with a similar ordering temperature, such as some of the underdoped iron-based superconductors where band folding due to the spin density wave is often hard to observe when close to the optimal doping<sup>88,89</sup>. Yet, the flat band in  $\text{CsCr}_3\text{Sb}_5$  is clearly participating in the low-temperature order, evident in its shift away from  $E_F$  and its coupling with spin excitations. Hence,  $\text{CsCr}_3\text{Sb}_5$  appears to exist in a regime that is also close to the potential quantum critical point of the phase diagram but on the ordered side<sup>54–56</sup>, a place that is between the strong magnetically ordered kagome metals and  $\text{Ni}_3\text{In}$ . Recent theoretical studies have revealed that the flat bands in close proximity to  $E_F$  in  $\text{CsCr}_3\text{Sb}_5$  give rise to antiferromagnetic

spin fluctuations, suggesting the important role that these FBs play in this emergent order<sup>59</sup>. Interestingly, under the tuning knob of hydrostatic pressure, the competing phase in  $\text{CsCr}_3\text{Sb}_5$  is suppressed and superconductivity emerges. This drastic response to pressure, together with the observed FB near  $E_F$ , and its potential association with spin excitations, suggests that  $\text{CsCr}_3\text{Sb}_5$  opens up access to a previously experimentally unexplored regime in the overarching phase diagram of kagome metals that offers intriguing insights into novel phases associated with the topological flat band physics.

## Methods

### Crystal growth and characterization

The  $\text{CsCr}_3\text{Sb}_5$  single crystals were grown using the self-flux method. Cs (Solid, Alfa 99.8%), Cr (Powder, Alfa 99.95%), and Sb (Powder, Alfa 99.5%) in a molar ratio of 12:3:30 were mixed. The mixture was loaded into an alumina crucible, and sealed in a Ta/Nb tube by arc welding under an argon atmosphere with one atmospheric pressure. The tube was sealed in an evacuated quartz tube to protect Ta/Nb from  $\text{O}_2$ . The Ta/Nb tube was used to prevent the reaction between Cs vapor and the quartz tube, but Cs can still react slightly with Ta/Nb. The sample was heated to 850–905 °C within 12 h, kept for 50 h, cooled to 580–600 °C at a rate of 1.5–3 °C /h, and cooled to room temperature naturally. Thin crystalline flakes can be found in the melts, and the crystals are stable to water and the air. The sample size for this experiment is about  $1 \times 1 \text{ mm}^2$ .

### ARPES measurements

ARPES experiments were performed at the MAESTRO beamline of the Advanced Light Source and beamline 5-2 of the Stanford Synchrotron Radiation Lightsource. The MAESTRO beamline is equipped with a Scienta electron analyzer in a home-designed deflector mode and uses a beamspot of  $10 \times 10 \mu\text{m}^2$ . SSRL beamline 5-2 employs a DA30 electron analyzer with a  $10 \times 30 \mu\text{m}^2$  beamspot. The angular resolution was set to 0.1° and the total energy resolution to  $\leq 20$  meV. All samples were cleaved in situ at 10 K, and measurements were conducted in ultra-high vacuum (base pressure  $< 5 \times 10^{-11}$  Torr). In figures, the error bars denote the standard errors  $1\sigma$  in the fitted parameters, calculated as the square root of the diagonal elements of the covariance matrix returned by the least-squares fitting procedure.

### RIXS measurements

We conducted Cr  $L_3$ -edge RIXS measurements using the AGM-AGS spectrometer at beamline 41A<sup>90</sup> of the Taiwan Photon Source, National Synchrotron Radiation Research Center, Taiwan. The total RIXS energy resolution was 26 meV, determined by the spectral full width at half maximum of the elastic scattering with  $\sigma$  polarization. The angle between the incident and scattered X-rays was fixed at 90° for both incident-energy-dependent and temperature-dependent RIXS measurements, with unresolved polarization of scattered X-rays. Prior to XAS and RIXS measurements, crystallographic axes were aligned using hard X-ray diffraction with a specially designed tilting adjustment holder. Subsequently, samples were cleaved in air to expose a (001) surface. X-ray absorption spectra were acquired using a photodiode in fluorescence yield mode. The error bars of fitting constants represent the  $1\sigma$  standard errors on the fit parameters.

### DFT calculations

All DFT calculations were performed with the Vienna ab initio simulation package (VASP) code<sup>91,92</sup>, with Perdew-Burke-Ernzerhof exchange-correlation functional<sup>93</sup>. The energy cutoff of the plane wave basis is 450 eV, and the 3D Brillouin zone is sampled with a k-point mesh of  $11 \times 11 \times 5$ . All atoms are relaxed until residual force is under 0.01 eV/Å. A tight-binding model of 31 orbitals is fitted from DFT

results with Wannier functions, as implemented in the Wannier90 package<sup>94</sup>.

### XRD measurements

The structure information of the crystal was investigated at ORNL using a Rigaku XtaLAB PRO diffractometer equipped with a HyPix-6000HE detector on single crystals with a dimension of  $0.1 \times 0.1 \times 0.01 \text{ mm}^3$ . A molybdenum anode was used to generate x-rays with wavelength  $\lambda = 0.7107 \text{ \AA}$ . The samples were cooled by a Helium gas flow provided by an Oxford N-Helix cryosystem.

### SEM and EDS measurements

The chemical composition is measured in the FEI Quanta 400 is a high-resolution field emission scanning electron microscope. It is equipped with SE, backscatter, and EDS detectors, and can operate in high vac, low vac, and Wet modes. It is also equipped with a cooling stage.

### Data availability

All data needed to evaluate the conclusions are present in the paper and supplementary materials. Additional data are available from the corresponding authors on request.

### Code availability

The band structure calculations and RIXS used in this study are available from the corresponding authors upon request.

### References

- Checkelsky, J. G., Bernevig, B. A., Coleman, P., Si, Q. & Paschen, S. Flat bands, strange metals and the kondo effect. *Nat. Rev. Mater.* **9**, 509–526 (2024).
- Das, I. et al. Symmetry-broken chern insulators and rashba-like landau-level crossings in magic-angle bilayer graphene. *Nat. Phys.* **17**, 710–714 (2021).
- Xie, Y. et al. Fractional chern insulators in magic-angle twisted bilayer graphene. *Nature* **600**, 439–443 (2021).
- Lisi, S. et al. Observation of flat bands in twisted bilayer graphene. *Nat. Phys.* **17**, 189–193 (2020).
- Kirchner, S. et al. Colloquium: Heavy-electron quantum criticality and single-particle spectroscopy. *Rev. Mod. Phys.* **92**, 011002 (2020).
- Fernandes, R. M. et al. Iron pnictides and chalcogenides: a new paradigm for superconductivity. *Nature* **601**, 35–44 (2022).
- Iglovikov, V. I., Hébert, F., Grémaud, B., Batrouni, G. G. & Scalettar, R. T. Superconducting transitions in flat-band systems. *Phys. Rev. B* **90**, 094506 (2014).
- Bistritzer, R. & MacDonald, A. H. Moiré bands in twisted double-layer graphene. *Proc. Natl. Acad. Sci. USA* **108**, 12233–12237 (2011).
- Cao, Y. et al. Unconventional superconductivity in magic-angle graphene superlattices. *Nature* **556**, 43–50 (2018).
- Tian, H. et al. Evidence for dirac flat band superconductivity enabled by quantum geometry. *Nature* **614**, 440–444 (2023).
- Sutherland, B. Localization of electronic wave functions due to local topology. *Phys. Rev. B Condens. Matter* **34**, 5208–5211 (1986).
- Lieb, E. H. Two theorems on the hubbard model. *Phys. Rev. Lett.* **62**, 1201–1204 (1989).
- Essafi, K., Jaubert, L. D. C. & Udagawa, M. Flat bands and dirac cones in breathing lattices. *J. Phys. Condens. Matter* **29**, 315802 (2017).
- Regnault, N. et al. Catalogue of flat-band stoichiometric materials. *Nature* **603**, 824–828 (2022).
- Călugăru, D. et al. General construction and topological classification of crystalline flat bands. *Nat. Phys.* **18**, 185–189 (2022).
- Ye, L. et al. Massive dirac fermions in a ferromagnetic kagome metal:FeSn. *Nature* **555**, 638–642 (2018).

17. Kang, M. et al. Topological flat bands in frustrated kagome lattice CoSn. *Nat. Commun.* **11**, 4004 (2020).

18. Liu, Z. et al. Orbital-selective dirac fermions and extremely flat bands in frustrated kagome-lattice metal CoSn. *Nat. Commun.* **11**, 4002 (2020).

19. Kang, M. et al. Dirac fermions and flat bands in the ideal kagome metal FeSn. *Nat. Mater.* **19**, 163–169 (2020).

20. Lin, Z. et al. Dirac fermions in antiferromagnetic FeSn kagome lattices with combined space inversion and time-reversal symmetry. *Phys. Rev. B Condens. Matter* **102**, 155103 (2020).

21. Teng, X. et al. Discovery of charge density wave in a kagome lattice antiferromagnet. *Nature* **609**, 490–495 (2022).

22. Yin, J.-X. et al. Discovery of charge order and corresponding edge state in kagome magnet FeGe. *Phys. Rev. Lett.* **129**, 166401 (2022).

23. Teng, X. et al. Magnetism and charge density wave order in kagome FeGe. *Nat. Phys.* **19**, 814–822 (2023).

24. Ortiz, B. R. et al. New kagome prototype materials: discovery of  $KV_3Sb_5$ ,  $RbV_3Sb_5$ , and  $CsV_3Sb_5$ . *Phys. Rev. Mater.* **3**, 094407 (2019).

25. Jiang, Y.-X. et al. Unconventional chiral charge order in kagome superconductor  $KV_3Sb_5$ . *Nat. Mater.* **20**, 1353–1357 (2021).

26. Li, H. et al. Observation of unconventional charge density wave without acoustic phonon anomaly in kagome superconductors  $AV_3Sb_5$  ( $A=Rb, Cs$ ). *Phys. Rev. X* **11**, 031050 (2021).

27. Ortiz, B. R. et al. Superconductivity in the  $Z_2$  kagome metal  $KV_3Sb_5$ . *Phys. Rev. Mater.* **5**, 034801 (2021).

28. Zhao, H. et al. Cascade of correlated electron states in the kagome superconductor  $CsV_3Sb_5$ . *Nature* **599**, 216–221 (2021).

29. Hu, Y. et al. Rich nature of van hove singularities in kagome superconductor  $CsV_3Sb_5$ . *Nat. Commun.* **13**, 2220 (2022).

30. Kato, T. et al. Polarity-dependent charge density wave in the kagome superconductor  $CsV_3Sb_5$ . *Phys. Rev. B Condens. Matter* **106**, L121112 (2022).

31. Zheng, L. et al. Emergent charge order in pressurized kagome superconductor  $CsV_3Sb_5$ . *Nature* **611**, 682–687 (2022).

32. Werhahn, D. et al. The kagomé metals  $RbTi_3Bi_5$  and  $CsTi_3Bi_5$ . *Zeitschrift für Naturforschung B* **77**, 757–764 (2022).

33. Yang, H. et al. Superconductivity and nematic order in a new titanium-based kagome metal  $CsTi_3Bi_5$  without charge density wave order. *Nat. Commun.* **15**, 9262 (2024).

34. Liu, B. et al. Tunable van hove singularity without structural instability in kagome metal  $CsTi_3Bi_5$ . *Phys. Rev. Lett.* **131**, 026701 (2023).

35. Hu, Y. et al. Non-trivial band topology and orbital-selective electronic nematicity in a titanium-based kagome superconductor. *Nat. Phys.* **19**, 1827–1833 (2023).

36. Venturini, G., Idrissi, B. E. & Malaman, B. Magnetic properties of  $RMn_6Sn_6$  ( $R = Sc, Y, Gd-Tm, Lu$ ) compounds with  $HfFe_6Ge_6$  type structure. *J. Magn. Magn. Mater.* **94**, 35–42 (1991).

37. Yin, J.-X. et al. Quantum-limit chern topological magnetism in  $TbMn_6Sn_6$ . *Nature* **583**, 533–536 (2020).

38. Li, M. et al. Dirac cone, flat band and saddle point in kagome magnet  $YMn_6Sn_6$ . *Nat. Commun.* **12**, 3129 (2021).

39. Peng, S. et al. Realizing kagome band structure in Two-Dimensional kagome surface states of  $RV_6Sn_6$  ( $R=Gd, Ho$ ). *Phys. Rev. Lett.* **127**, 266401 (2021).

40. Rosenberg, E. et al. Uniaxial ferromagnetism in the kagome metal  $TbV_6Sn_6$ . *Phys. Rev. B Condens. Matter* **106**, 115139 (2022).

41. Cheng, Z.-J. et al. Visualization of tunable weyl line in A-A stacking kagome magnets. *Adv. Mater.* **35**, e2205927 (2023).

42. Lee, S. et al. Nature of charge density wave in kagome metal  $ScV_6Sn_6$ . *Npj Quantum Mater.* **9**, 15 (2024).

43. Hu, Y. et al. Phonon promoted charge density wave in topological kagome metal  $ScV_6Sn_6$ . *Nat. Commun.* **15**, 1658 (2024).

44. Cheng, S. et al. Nanoscale visualization and spectral fingerprints of the charge order in  $ScV_6Sn_6$  distinct from other kagome metals. *Npj Quantum Mater.* **9**, 14 (2024).

45. Wu, C., Bergman, D., Balents, L. & Das Sarma, S. Flat bands and wigner crystallization in the honeycomb optical lattice. *Phys. Rev. Lett.* **99**, 070401 (2007).

46. Mielke, A. Ferromagnetic ground states for the hubbard model on line graphs. *J. Phys. A Math. Gen.* **24**, L73 (1991).

47. Tasaki, H. Ferromagnetism in the hubbard models with degenerate single-electron ground states. *Phys. Rev. Lett.* **69**, 1608–1611 (1992).

48. Miyahara, S., Kusuta, S. & Furukawa, N. BCS theory on a flat band lattice. *Phys. C Supercond.* **460-462**, 1145–1146 (2007).

49. Zhang, S., Hung, H.-H. & Wu, C. Proposed realization of itinerant ferromagnetism in optical lattices. *Phys. Rev. A* **82**, 053618 (2010).

50. Aoki, H. Theoretical possibilities for flat band superconductivity. *J. Supercond. Novel Magn.* **33**, 2341–2346 (2020).

51. Tang, E., Mei, J.-W. & Wen, X.-G. High-temperature fractional quantum hall states. *Phys. Rev. Lett.* **106**, 236802 (2011).

52. Bergman, D. L., Wu, C. & Balents, L. Band touching from real-space topology in frustrated hopping models. *Phys. Rev. B Condens. Matter* **78**, 125104 (2008).

53. Ye, L. et al. Hopping frustration-induced flat band and strange metallicity in a kagome metal. *Nat. Phys.* **20**, 610–614 (2024).

54. Hu, H. & Si, Q. Coupled topological flat and wide bands: Quasi-particle formation and destruction. *Sci. Adv.* **9**, eadg0028 (2023).

55. Chen, L. et al. Emergent flat band and topological kondo semimetal driven by orbital-selective correlations. *Nat. Commun.* **15**, 5242 (2024).

56. Chen, L. et al. Metallic quantum criticality enabled by flat bands in a kagome lattice. Preprint at <https://doi.org/10.48550/arXiv.2307.09431> (2023).

57. Liu, Y. et al. Superconductivity under pressure in a chromium-based kagome metal. *Nature* **632**, 1032 (2024).

58. Xu, C. et al. Altermagnetic ground state in distorted kagome metal  $CsCr_3Sb_5$ . *Nat. Commun.* **16**, 3114 (2025).

59. Wu, S. et al. Flat-band enhanced antiferromagnetic fluctuations and superconductivity in pressurized  $CsCr_3Sb_5$ . *Nat. Commun.* **16**, 1375 (2025).

60. Armitage, N. P., Fournier, P. & Greene, R. L. Progress and perspectives on electron-doped cuprates. *Rev. Mod. Phys.* **82**, 2421–2487 (2010).

61. Dai, P. Antiferromagnetic order and spin dynamics in iron-based superconductors. *Rev. Mod. Phys.* **87**, 855–896 (2015).

62. Scalapino, D. J. A common thread: The pairing interaction for unconventional superconductors. *Rev. Mod. Phys.* **84**, 1383–1417 (2012).

63. Si, Q. & Hussey, N. E. Iron-based superconductors: Teenage, complex, challenging. *Phys. Today* **76**, 34–34 (2023).

64. Yi, M. et al. Observation of temperature-induced crossover to an orbital-selective mott phase in  $A_xFe_{2-y}Se_2$  ( $A=K, Rb$ ) superconductors. *Phys. Rev. Lett.* **110**, 067003 (2013).

65. Huang, J. et al. Correlation-driven electronic reconstruction in  $FeTe_{1-x}Se_x$ . *Commun. Phys.* **5**, 29 (2022).

66. Yi, M. et al. Observation of universal strong orbital-dependent correlation effects in iron chalcogenides. *Nat. Commun.* **6**, 7777 (2015).

67. Huang, J., Guo, Y. & Yi, M. Electron correlations and nematicity in the Iron-Based superconductors. *Synchrotron Radiat. News* **36**, 30–38 (2023).

68. Samanta, S. et al. Emergence of flat bands and ferromagnetic fluctuations via orbital-selective electron correlations in mn-based kagome metal. *Nat. Commun.* **15**, 5376 (2024).

69. Neupane, M. et al. Observation of a novel orbital selective mott transition in  $Ca_{1.8}Sr_{0.2}RuO_4$ . *Phys. Rev. Lett.* **103**, 097001 (2009).

70. Jeong, M. Y. et al. Crucial role of out-of-plane sb p orbitals in van hove singularity formation and electronic correlations in the superconducting kagome metal  $\text{CsV}_3\text{Sb}_5$ . *Phys. Rev. B Condens. Matter* **105**, 235145 (2022).
71. Ament, L. J. P., van Veenendaal, M., Devvereaux, T. P., Hill, J. P. & van den Brink, J. Resonant inelastic x-ray scattering studies of elementary excitations. *Rev. Mod. Phys.* **83**, 705–767 (2011).
72. Nozières, P. & Abrahams, E. Threshold singularities of the x-ray raman scattering in metals. *Phys. Rev. B* **10**, 3099–3112 (1974).
73. Tacon, M. L. et al. Intense paramagnon excitations in a large family of high-temperature superconductors. *Nat. Phys.* **7**, 725–730 (2011).
74. Dean, M. et al. Persistence of magnetic excitations in  $\text{La}_{2-x}\text{Sr}_x\text{CuO}_4$  from the undoped insulator to the heavily overdoped non-superconducting metal. *Nat. Mater.* **12**, 1019–1023 (2013).
75. Jia, C., Wohlfeld, K., Wang, Y., Moritz, B. & Devvereaux, T. P. Using rixs to uncover elementary charge and spin excitations. *Phys. Rev. X* **6**, 021020 (2016).
76. Benjamin, D., Klich, I. & Demler, E. Single-band model of resonant inelastic x-ray scattering by quasiparticles in high- $T_c$  cuprate superconductors. *Phys. Rev. Lett.* **112**, 247002 (2014).
77. Coldea, R. et al. Spin waves and electronic interactions in  $\text{La}_2\text{CuO}_4$ . *Phys. Rev. Lett.* **86**, 5377–5380 (2001).
78. Zhou, K.-J. et al. Persistent high-energy spin excitations in iron-pnictide superconductors. *Nat. Commun.* **4**, 1470 (2013).
79. Lu, X. et al. Spin-excitation anisotropy in the nematic state of det-winned fese. *Nat. Phys.* **18**, 806–812 (2022).
80. Xie, F. et al. Electron correlations in the kagome flat band metal  $\text{CsCr}_3\text{Sb}_5$ . *Phys. Rev. Research* **7**, L022061 (2025).
81. Wang, Y. Heavy fermions in frustrated hund's metal with portions of incipient flat bands. *Phys. Rev. B* **111**, 035127 (2025).
82. Huang, J. et al. Non-Fermi liquid behaviour in a correlated flat-band pyrochlore lattice. *Nat. Phys.* **20**, 603–609 (2024).
83. Teng, X. et al. Spin-charge-lattice coupling across the charge density wave transition in a kagome lattice antiferromagnet. *Phys. Rev. Lett.* **133**, 046502 (2024).
84. Klemm, M. L. et al. Vacancy-induced suppression of charge density wave order and its impact on magnetic order in kagome antiferromagnet FeGe. *Nat. Commun.* **16**, 3313 (2025).
85. Mazet, T., Isnard, O. & Malaman, B. A study of the new  $\text{Yb}_{0.6}\text{Fe}_6\text{Sn}_3$  compound by neutron diffraction,  $^{57}\text{Fe}$  and  $^{119}\text{Sn}$  mössbauer spectroscopy experiments. *J. Magn. Magn. Mater.* **241**, 51–59 (2002).
86. Ji Seop, Oh et al. Disentangling the intertwined orders in a magnetic kagome metal. *Sci. Adv.* **11**, ead2195 (2025).
87. Ren, Z. et al. Persistent flat band splitting and strong selective band renormalization in a kagome magnet thin film. *Nat. Commun.* **15**, 9376 (2024).
88. Ge, Q. Q. et al. Anisotropic but nodeless superconducting gap in the presence of Spin-Density wave in Iron-Pnictide superconductor  $\text{NaFe}_{1-x}\text{Co}_x\text{As}$ . *Phys. Rev. X* **3**, 011020 (2013).
89. Liu, C. et al. Evidence for a lifshitz transition in electron-doped iron arsenic superconductors at the onset of superconductivity. *Nat. Phys.* **6**, 419–423 (2010).
90. Singh, A. et al. Development of the soft X-ray AGM-AGS RIXS beamline at the taiwan photon source. *J. Synchrotron Radiat.* **28**, 977 (2021).
91. Kresse, G. & Furthmüller, J. Efficient iterative schemes for ab initio total-energy calculations using a plane-wave basis set. *Phys. Rev. B* **54**, 11169–11186 (1996).
92. Kresse, G. & Joubert, D. From ultrasoft pseudopotentials to the projector augmented-wave method. *Phys. Rev. B* **59**, 1758–1775 (1999).
93. Perdew, J. P., Burke, K. & Ernzerhof, M. Generalized Gradient Approximation Made Simple. *Phys. Rev. Lett.* **77**, 3865–3868 (1996).
94. Pizzi, G. et al. Wannier90 as a community code: new features and applications. *J. Phys. Condens. Matter* **32**, 165902 (2020).

## Acknowledgements

The single-crystal synthesis work and RIXS experiments at Rice were supported by the U.S. DOE, BES under Grant No. DE-SC0012311 (P.D.). Part of the materials characterization efforts at Rice is supported by the Robert A. Welch Foundation Grant No. C-1839 (P.D.). The ARPES work at Rice University was supported by the U.S. DOE grant No. DE-SC0021421, the Gordon and Betty Moore Foundation's EPIQS Initiative through grant No. GBMF9470 and the Robert A. Welch Foundation Grant No. C-2175 (M.Y.). Y.G. is supported in part by an ALS Doctoral Fellowship in Residence. Y.Z. is partially supported by the Air Force Office of Scientific Research (AFOSR) Grant No. FA9550-21-1-0343. The RIXS work in Taiwan is partially supported by the National Science and Technology Council of Taiwan under Grant No. NSTC 112-2112-M-213-026-MY3 (D.J.H.) The theory work at Rice is supported by the NSF Grant No. DMR-2220603 (F.X. and Y.F.), by the AFOSR Grant No. FA9550-21-1-0356 (Y.W.), and by the Robert A. Welch Foundation Grant No. C-1411 (Q.S.), and by the Vannevar Bush Faculty Fellowship, ONR-VB N00014-23-1-2870 (Q.S.). Computational modeling was supported by the Office of Naval Research Grant N00014-22-1-2753 (Y.H. and B.I.Y.). The transport and thermodynamic measurements at UW were supported by the Air Force Office of Scientific Research (AFOSR) under Award No. FA2386-21-1-4060 and the David Lucile Packard Foundation (J.H.C.). Work at the University of California, Berkeley and Lawrence Berkeley National Laboratory was funded by the U.S. DOE, Office of Science, Office of Basic Energy Sciences, Materials Sciences and Engineering Division under Contract No. DE-AC02-05CH11231 (Quantum Materials Program KC2202). J.S.O., R.J.B., and M.Y. acknowledge the support from National Science Foundation (NSF) grants Nos. DMR-1921798 and DMR-2324032. M.H. and D.L. acknowledge the support of the U.S. Department of Energy, Office of Science, Office of Basic Energy Sciences, Division of Materials Sciences and Engineering, under contract DE-AC02-76SF00515. A.F. acknowledges the support of the National Science and Technology Council of Taiwan under Grant No. 113-2112-M-007-033, the Japan Society for the Promotion of Science under Grant No. JP22K03535, and the Yushan Fellow Program of the Ministry of Education of Taiwan. This research used resources of the Advanced Light Source, which is a DOE Office of Science User Facility under contract no. DE-AC02-05CH11231. Use of the Stanford Synchrotron Radiation Lightsource, SLAC National Accelerator Laboratory, is supported by the U.S. Department of Energy, Office of Science, Office of Basic Energy Sciences under Contract No. DE-AC02-76SF00515. A portion of this research used resources at the Spallation Neutron Source, a DOE Office of Science User Facility operated by Oak Ridge National Laboratory.

## Author contributions

P.D. initiated this project. P.D., M.Y., D.J.H., and Q.S. oversaw the project. Y.G., J.S.O., Z.R., Y.Z., Z.Y., A.B. (Ananya Biswas) and C.H. carried out the ARPES measurements with the help of E.R., A.B. (Aaron Bostwick), C.J., M.H., D.L., J.K., and R.J.B. The ARPES data were analyzed by Y.G. and H.W. with the help of M.Y. H.Y.H., J.O., and G.C. conducted the RIXS measurements with the help of D.J.H., A.F., and C.T.C. H.Y.H. and D.J.H. analyzed the RIXS data with the help of Z.W. and X.L. Single crystals were synthesized by Z.W. and B.G. under the guidance of P.D. and G.H.C.  $U(1)$  auxiliary-spin calculations were carried out by F.X., Y.F., Y.W., and Q.S. Density-functional theory calculations and tight-binding model fitting were carried out by Y.H. under the guidance of B.Y. Transport measurements were carried out by Z.L. and J.C. F.Y. carried out X-ray diffraction measurements. Y.G., Z.W., M.Y., D.J.H., and P.D. wrote the paper with input from all co-authors.

## Competing interests

The authors declare no competing interests.

## Additional information

**Supplementary information** The online version contains supplementary material available at <https://doi.org/10.1038/s41467-025-62298-5>.

**Correspondence** and requests for materials should be addressed to Di-Jing Huang, Qimiao Si, Ming Yi or Pengcheng Dai.

**Peer review information** *Nature Communications* thanks the anonymous reviewers for their contribution to the peer review of this work. A peer review file is available.

**Reprints and permissions information** is available at <http://www.nature.com/reprints>

**Publisher's note** Springer Nature remains neutral with regard to jurisdictional claims in published maps and institutional affiliations.

**Open Access** This article is licensed under a Creative Commons Attribution-NonCommercial-NoDerivatives 4.0 International License, which permits any non-commercial use, sharing, distribution and reproduction in any medium or format, as long as you give appropriate credit to the original author(s) and the source, provide a link to the Creative Commons licence, and indicate if you modified the licensed material. You do not have permission under this licence to share adapted material derived from this article or parts of it. The images or other third party material in this article are included in the article's Creative Commons licence, unless indicated otherwise in a credit line to the material. If material is not included in the article's Creative Commons licence and your intended use is not permitted by statutory regulation or exceeds the permitted use, you will need to obtain permission directly from the copyright holder. To view a copy of this licence, visit <http://creativecommons.org/licenses/by-nc-nd/4.0/>.

© The Author(s) 2025

<sup>1</sup>Department of Physics and Astronomy, Rice University, Houston, USA. <sup>2</sup>National Synchrotron Radiation Research Center, Hsinchu, Taiwan. <sup>3</sup>Department of Materials Science and NanoEngineering, Rice University, Houston, Texas, USA. <sup>4</sup>Department of Physics, University of California, Berkeley, California, USA. <sup>5</sup>Department of Applied Physics, Sookmyung Women's University, Seoul, Republic of Korea. <sup>6</sup>Institute of Advanced Materials and Systems, Sookmyung Women's University, Seoul, Republic of Korea. <sup>7</sup>Neutron Scattering Division, Oak Ridge National Laboratory, Oak Ridge, TN, USA. <sup>8</sup>Center for Advanced Quantum Studies, School of Physics and Astronomy, Beijing Normal University, Beijing, China. <sup>9</sup>Department of Physics, University of Washington, Washington, USA. <sup>10</sup>Applied Physics Graduate Program, Smalley-Curl Institute, Rice University, Houston, Texas, USA. <sup>11</sup>Advanced Light Source, Lawrence Berkeley National Laboratory, Berkeley, California, USA. <sup>12</sup>Stanford Synchrotron Radiation Lightsource, SLAC National Accelerator Laboratory, Menlo Park, California, USA. <sup>13</sup>Department of Electrical and Computer Engineering, Rice University, Houston, Texas, USA. <sup>14</sup>Smalley-Curl Institute, Rice University, Houston, Texas, USA. <sup>15</sup>School of Physics, Zhejiang University, Hangzhou, China. <sup>16</sup>Center for Quantum Science and Technology and Department of Physics, National Tsing Hua University, Hsinchu, Taiwan. <sup>17</sup>Department of Physics, University of Tokyo, Bunkyo-Ku, Tokyo, Japan. <sup>18</sup>Department of Physics, National Tsing Hua University, Hsinchu, Taiwan. <sup>19</sup>Department of Electrophysics, National Yang Ming Chiao Tung University, Hsinchu, Taiwan. <sup>20</sup>These authors contributed equally: Zehao Wang, Yucheng Guo, Hsiao-Yu Huang, Fang Xie.  e-mail: [djhuang@nsrrc.org.tw](mailto:djhuang@nsrrc.org.tw); [qmsi@rice.edu](mailto:qmsi@rice.edu); [mingyi@rice.edu](mailto:mingyi@rice.edu); [pdai@rice.edu](mailto:pdai@rice.edu)